Nanoscale Advances

ROYAL SOCIETY OF CHEMISTRY

PAPER

View Article Online
View Journal | View Issue

Cite this: *Nanoscale Adv.*, 2025, 7, 4679

Assessing $B_{12}N_{12}$ and $Al_{12}N_{12}$ nanocages as potential vehicles for 1-(phthalazin-1(2*H*)-one) [(pyridin-2-yl)ethylidene]hydrazine, against onchocerciasis: a DFT study†

Remi Nkeih Tamighang,[a] Stanley Numbonui Tasheh, *[a] Nyiang Kennet Nkungli, [a] Godfred Ayimele Aponglen,[ab] Numbonui Angela Beri,[a] Rajesh Haldhar *[c] and Julius Numbonui Ghogomu *[ad]

This work explores the potential of $B_{12}N_{12}$ and $Al_{12}N_{12}$ nanocages as carriers for 1-(phthalazin-1(2*H*)-one) [(pyridin-2-yl)ethylidene]hydrazone (**APN**). Density functional theory (DFT) calculations at M06/def2-SVP were conducted for energy minimization and at M06/def2-TZVP level for property calculations. Molecular electrostatic surface potential (ESP) analysis of **APN** identified two potential adsorption sites: the pyridine nitrogen (**confA**) and the azomethine nitrogen (**confB**). Thermochemical analysis indicates that the **APN**-nanocage complexes are energetically favorable, spontaneous and exothermic with **confA** complexes exhibiting the highest stability. Global reactivity studies indicate that complexation especially *via* **confA** significantly presents enhanced reactivity as evidenced by their lower HOMO–LUMO energy gaps and favourable electron transfer properties. QTAIM and NCI analyses show that the main interactions in the complexes are intermediate and non-covalent. Drug likeness analysis was equally performed and **APN** has a promising drug-like profile and could be a suitable candidate for further development as an orally bioavailable drug. Conclusively, both nanocages show promise as carriers for **APN** in the treatment of onchocerciasis.

Received 15th April 2025
Accepted 19th June 2025

DOI: 10.1039/d5na00360a

rsc.li/nanoscale-advances

1. Introduction

Onchocerciasis (subcutaneous filariasis) arises from infection by the parasitic worm *Onchocerca volvulus*.[1,2] It is characterized by the presence of clinical manifestations such as cutaneous lesions and ocular manifestations known as river blindness.[1,2] Its transmission to humans occurs *via* the bites of the black fly (*Simulium damnosum*), a species known to breed in rapid-flowing bodies of water.[1,3,4] According to the 2015 WHO report, the African continent is the most vulnerable to river blindness and associated skin lesions, with an estimated incidence of approximately 35 million cases of *Onchocerca volvulus* infections.[5,6] Among the affected individuals, approximately 300 000 people are afflicted with blindness, while around 800 000 individuals experience varying degrees of visual impairment.[6,7] Onchocerciasis is ranked as the second most prevalent infectious cause of blindness after trachoma.[5] Furthermore, this disease is linked to reduced life expectancy and elevated mortality rates among those infected, as well as social stigmatization of both affected individuals and their families.[2]

Due to the significant impact of onchocerciasis, various international organizations and donor groups have prioritized control measures for the disease.[5] Over the last 40 years, extensive regional and local interventions have been implemented, particularly through the mass distribution of mectizan (ivermectin).[6,8] While these efforts have effectively controlled the disease, they have not yet led to its eradication.[5,9] Mectizan is highly effective against microfilariae but does not significantly affect macrofilariae.[7] A yearly dose of mectizan over 15 to 18 years can potentially eliminate microfilariae in humans and interrupt transmission. However, this lengthy treatment regimen may lead to patient noncompliance and the risk of drug resistance. Recently, mectizan resistance has been observed in parasitic nematodes in veterinary contexts,[9] raising concerns about its potential spread to the human strain, *Onchocerca volvulus*.[8]

[a]*Department of Chemistry, Faculty of Science, The University of Bamenda, P.O. Box 39, Bambili-Bamenda, Cameroon. E-mail: tashehstanley@uniba.cm; ghogsjuju@hotmail.com*

[b]*Department of Chemistry, Faculty of Science, University of Buea, P.O. Box 63, Buea, Cameroon*

[c]*School of Chemical Engineering, Yeungnam University, Gyeongsan – 38541, Republic of Korea. E-mail: rajeshhaldhar.lpu@gmail.com*

[d]*Research Unit of Noxious Chemistry and Environmental Engineering, Department of Chemistry, Faculty of Science, University of Dschang, P.O. Box 67, Dschang, Cameroon*

† Electronic supplementary information (ESI) available: Additional tables constituting part of this work. Tables S1–S7 gives the optimized geometrical coordinates. See DOI: https://doi.org/10.1039/d5na00360a

These challenges highlight the urgent need for more effective anti-onchocercal drugs that can quickly target human *Onchocerca volvulus*. In response, several Schiff bases have been developed, including 1-(phthalazin-1(2*H*)-one)[(pyridin-2-yl) ethylidene]hydrazone (**APN**) (see Fig. 1), which has demonstrated significant micro- and macro-filaricidal activity, making it a promising candidate for anti-onchocercal treatment.[7] Despite this, its delivery mechanism and efficacy require further exploration. The lack of targeted delivery systems hinders the potential therapeutic impact of these compounds, necessitating innovative approaches to enhance drug bioavailability and effectiveness. Moreover, this targeted delivery can easily be achieved by using nanomaterials such as boron nitride ($\mathbf{B_{12}N_{12}}$) and aluminum nitride ($\mathbf{Al_{12}N_{12}}$) nanocages. $\mathbf{B_{12}N_{12}}$ is produced through an arc casting technique and identified *via* laser desorption TOF-MS.[10] $\mathbf{B_{12}N_{12}}$ has gained significant attention in research due to its remarkable characteristics, including oxidation resistance and an appropriate energy gap for optoelectronic properties.[11] Due to its structural stability, it is commonly utilized in various forms, including nanoclusters,[12] nanotubes,[13,14] nanosheets[15,16] and nanocages.[11,17] Due to the structural and molecular similarities between boron and aluminum atoms,[18] the $\mathbf{Al_{12}N_{12}}$ nanocage has equally received attention. Additionally, both $\mathbf{B_{12}N_{12}}$ and $\mathbf{Al_{12}N_{12}}$ nanocages consist of 8 6-sided and 6 4-sided rings, which are reportedly more stable than their $C_{12}N_{12}$ and C_{24} counterparts.[10,19] The polarity of the Al–N and B–N bonds in $\mathbf{Al_{12}N_{12}}$ and $\mathbf{B_{12}N_{12}}$, respectively, enhances the likelihood of biological molecules adsorbing onto their surfaces.

Although **APN** has exhibited notable micro- and macro-filaricidal activity against onchocerciasis, there has been no theoretical analysis of its interaction with $\mathbf{B_{12}N_{12}}$ and $\mathbf{Al_{12}N_{12}}$ nanocages as potential carrier molecules, warranting studies in this light. This study investigated the capability of $\mathbf{B_{12}N_{12}}$ and $\mathbf{Al_{12}N_{12}}$ nanocages as effective drug delivery systems for **APN** *via* DFT. The choice of these nanomaterials is due to their biocompatibility and non-toxicity in biomedical, therapeutic, and diagnostic applications.[10,15] To evaluate the effectiveness of $\mathbf{B_{12}N_{12}}$ and $\mathbf{Al_{12}N_{12}}$ nanocages as delivery agents for **APN**, geometry optimization of **APN** and its complexes with both nanocages was performed, followed by thermochemical analysis. Furthermore, the electronic parameters of the molecules were evaluated, alongside the drug-likeness parameters of **APN**. DFT was employed as it provides a cost-effective and efficient approach and the fact that it accounts for electron correlation.[20] The findings from this theoretical investigation could pave the way for future experimental studies to validate the predicted interactions between **APN** and the selected nanocages.

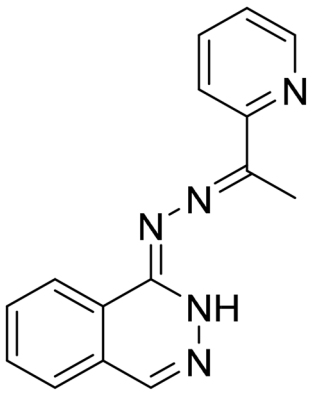

Fig. 1 Chemical structure of 1-(phthalazin-1(2*H*)-one)[(pyridin-2-yl) ethylidene]hydrazine (**APN**).

2. Computational details

The quantum computations here utilized the ORCA version 5.0.3 tool.[21] However, molecular orbitals for the molecular electrostatic surface potential (MESP) analysis were generated using ORCA version 3.0.1 (ref. 22) due to compatibility limitations with the visualization software. The MESP surfaces were visualized using Molekel 4.3,[23] which requires input files compatible only with earlier ORCA versions. To maintain consistency, single-point calculations in ORCA 3.0.1 were conducted at the same level of theory as those in ORCA 5.0.3. This approach ensured methodological uniformity while accommodating the technical requirements of the visualization tool. The input configurations were set up using Avogadro-1.1.1.[24] Geometry refinement then vibrational analyses were achieved through the M06 functional,[25] the def2-SVP basis set[26] and Grimme's D3 empirical dispersion correction. The M06 functional was selected based on its well-documented reliability in describing noncovalent interactions, thermochemistry and transition-metal bonding, which are critical features for accurately modelling nanocage–drug interactions. Specifically, M06 has demonstrated good performance in systems involving dispersion forces and charge transfer, as shown in previous benchmark studies.[27]

The resolution-of-identity (RI-J)[28] and chain-of-spheres (COSX) approximations, collectively termed RIJCOSX, were utilized to greatly speed up the geometry refinement and vibrational analysis while maintaining a high level of accuracy with only a slight loss. Vibrational analyses reveal that all refined geometries align with stable structures, as shown by the lack of imaginary frequencies.

Based on the optimized structures, the adsorption energies (E_{ads}) for all configurations were calculated. E_{ad} was determined using the supramolecular method, consequently the related basis set superposition error (BSSE) was corrected by means of the geometrical counterpoise (gCP)[29] method. The gCP method was used as it provides BSSE corrections comparable in magnitude and accuracy to the full counterpoise approach.[30] The computed thermodynamic properties of the complexes comprised enthalpy change (ΔH_{ad}), entropy change (ΔS_{ad}) and Gibbs free energy change (ΔG_{ad}) at 1 atm and 298.15 K using Shermo-v2.6 utility software[31] according to the following equations.

$$E_{ad} = E_{APN/Cage} - (E_{cage} + E_{APN}) + E_{BSSE} \quad (1)$$

$$\Delta H_{ad} = H_{APN/Cage} - (H_{cage} + H_{APN}) \quad (2)$$

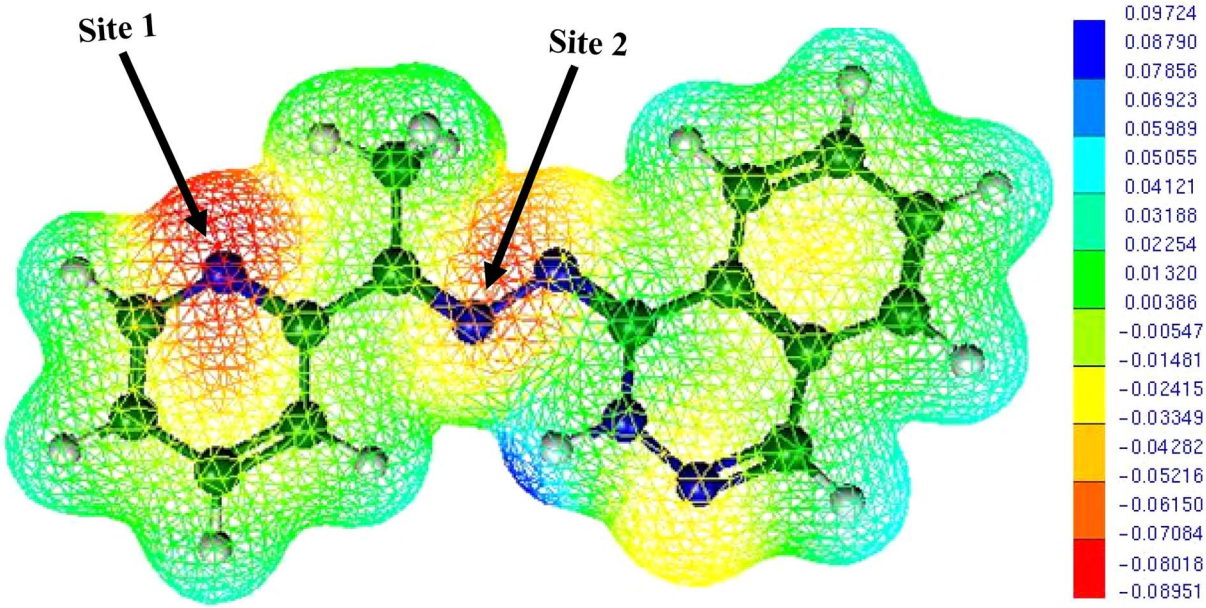

Fig. 2 Molecular electrostatic surface potential (MESP) map of **APN** at M06/def2-SVP level.

$$\Delta S_{ad} = S_{APN/Cage} - (S_{cage} + S_{APN}) \quad (3)$$

$$\Delta G_{ad} = \Delta H_{ad} - T\Delta S_{ad} \quad (4)$$

here E, G, H and S denote the over-all electronic energy, Gibb's free energy, enthalpy and entropy, respectively. E_{BSSE} refers to the basis set superposition error.

To analyse **APN's** adsorption behaviour on $\mathbf{B_{12}N_{12}}$ and $\mathbf{Al_{12}N_{12}}$ nanocages, single-point energies (SPEs) were achieved *via* the M06/def2-TZVP computational approach. The M06 density functional was selected for its reliability in predicting molecular energies and accurately describing weak intermolecular forces, which are critical for modelling adsorption processes involving noncovalent interactions.[25,32] From the SPEs, the energy gap (E_g), chemical hardness (η), maximum transferred charge (ΔN_{max}), chemical potential (μ) and the electrophilicity (ω) were computed according to eqn (5)–(9):

$$E_g = E_{LUMO} - E_{HOMO} \quad (5)$$

$$\mu = \frac{(E_{LUMO} + E_{HOMO})}{2} \quad (6)$$

$$\eta = \frac{(E_{LUMO} - E_{HOMO})}{2} \quad (7)$$

$$\omega = \frac{\mu^2}{2\eta} \quad (8)$$

$$\Delta N_{max} = \frac{-\mu}{\eta} \quad (9)$$

E_{HOMO} and E_{LUMO} signify the highest occupied molecular orbital and the lowest unoccupied molecular orbital energies, respectively.

The non-covalent interaction (NCI) index and quantum theory of atoms-in-molecules (QTAIM) studies were executed with Multiwfn 3.8,[33] using molecular orbitals obtained from SPE calculations. These methods helped map out the weak intermolecular forces governing drug-nanocage binding interactions. To assess **APN**'s suitability as a pharmaceutical candidate, we analyzed its absorption, distribution and safety profiles through SwissADME[34] and ADMETlab 3.0 (ref. 35) platforms.

3. Results and discussion

3.1 Optimized structures and molecular electrostatic surface potential (MESP) analysis

To identify favourable binding regions for **APN** on both nanocages the molecular electrostatic potential (ESP) surfaces were analysed. The MESP surface of **APN** (see Fig. 2) revealed two distinct nucleophilic sites primed for electrophilic interactions: pyridine nitrogen (site 1) and azomethine nitrogen (site 2). These electron-rich centres likely drive adsorption through electrostatic attraction to positively charged regions on the nanocage surfaces. The adsorption complexes formed at the two identified binding sites of **APN** were labelled as **confA** (site 1, pyridine nitrogen) and **confB** (site 2, azomethine nitrogen) to distinguish their structural configurations. Detailed geometric parameters, including refined Cartesian coordinates for all systems studied, are included in the ESI (see Tables S1–S7†).

The findings demonstrate that the optimal C=N bond lengths (B-Ls) at sites 1 and 2 in **APN** are determined to be 1.327 Å and 1.292 Å, respectively. Upon adsorption of **APN** onto the $\mathbf{B_{12}N_{12}}$ surface, these B-Ls increase to 1.345 Å (in **confA**) and 1.303 Å (in **confB**). The observed elongation in bond lengths indicates stronger **APN**/nanocages interactions. For example, the B–N bond in the pristine $\mathbf{B_{12}N_{12}}$ nanocage stretches from 1.435 Å to 1.570 Å in **confA** and 1.531 Å in **confB**. Similarly, the Al–N bond in the pristine $\mathbf{Al_{12}N_{12}}$ nanocage extends from 1.843 Å to 1.860 Å in **confA** and 1.873 Å in **confB** after **APN** adsorption.

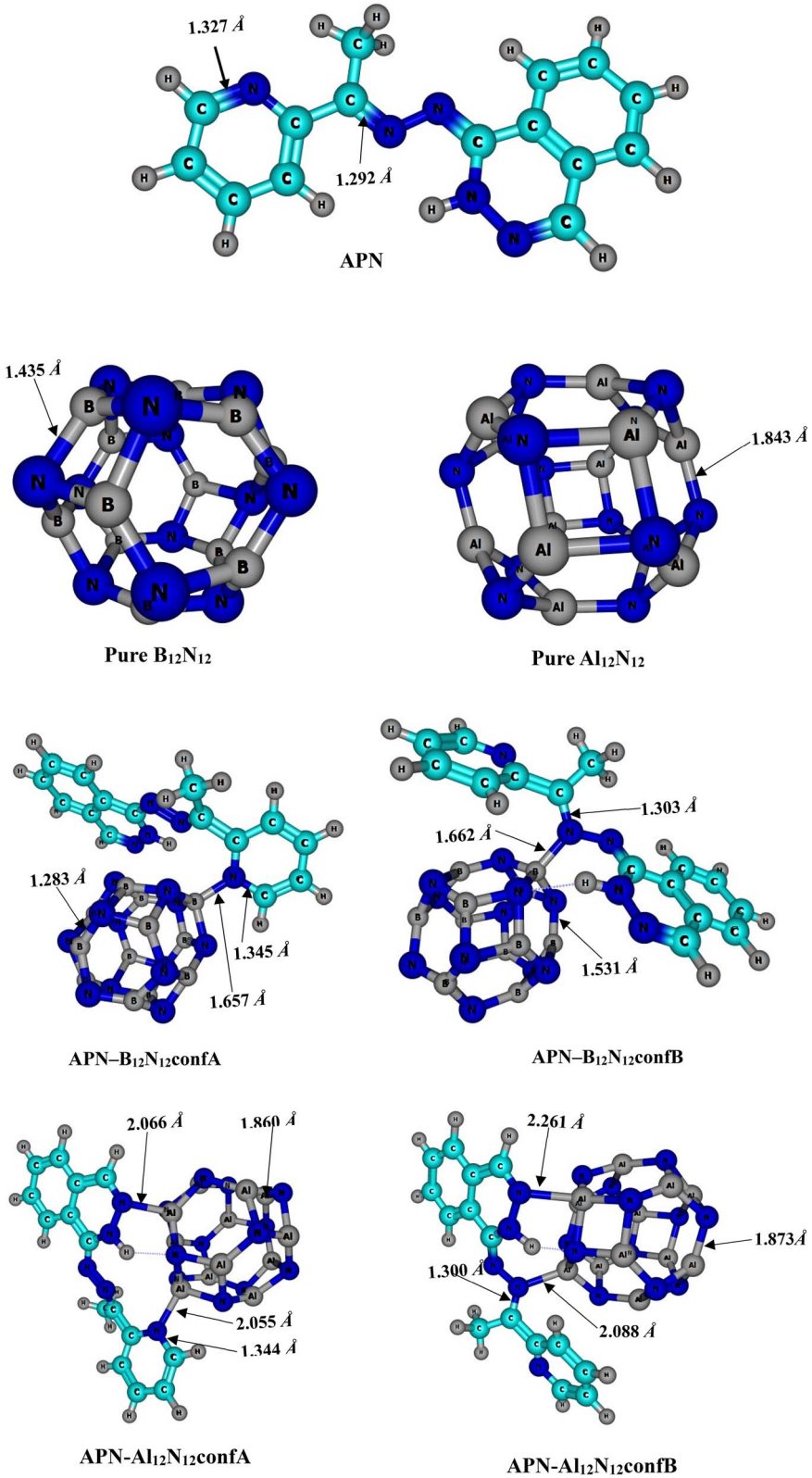

Fig. 3 Optimized structures APN and its complexes with $B_{12}N_{12}$ and $Al_{12}N_{12}$.

These changes in B-Ls point to structural distortions in the nanocages, likely caused by the adsorption process. The expansion of these bonds highlights the significant influence of **APN** on the nanocage geometry, reflecting the strength of the interactions at play. These structural changes are consistent with those reported elsewhere,[36] further supporting the potential adsorption of **APN** on the nanocages under investigation.

Table 1 Entropic term (TS), adsorption energy (E_{ad}), enthalpy changes (ΔH_{ad}), entropic variations ($T\Delta S_{ad}$) at 298.15 K and Gibb's free energy changes (ΔG_{ad}) of the studied compounds (all values are in kcal mol^{-1}) at M06/def2-TZVP level of theory

Molecule	TS	E_{ad}	ΔH_{ad}	$T\Delta S_{ad}$	ΔG_{ad}
APN	37.19	—	—	—	—
$B_{12}N_{12}$	27.26	—	—	—	—
APN–$B_{12}N_{12}$confA	49.88	−57.90	−29.81	−14.56	−15.25
APN–$B_{12}N_{12}$confB	50.46	−43.24	−26.81	−13.99	−12.82
$Al_{12}N_{12}$	39.39	—	—	—	—
APN–Al12N12confA	60.18	−34.99	−55.14	−16.40	−38.73
APN–Al12N12confB	60.41	−31.55	−42.12	−16.17	−25.95

Typically, bond lengths falling within the range of 1.0–3.5 Å are indicative of chemisorption, whereas those exceeding 3.5 Å usually point to physisorption.[37] In this study, the **APN–$B_{12}N_{12}$** B-Ls are measured at 1.657 Å (in **confA**) and 1.662 Å (in **confB**), as depicted in Fig. 3. Furthermore, the **APN–$Al_{12}N_{12}$** B-Ls are recorded to be 2.055 Å and 2.066 Å in **confA** and 2.088 Å and 2.261 Å in **confB**. These findings imply that the interaction between **APN** and both nanocages can be classified as chemisorption, with that of the **$B_{12}N_{12}$** nanocage being stronger.

3.2 Thermodynamic properties

Summarised in Table 1 are the values of the thermodynamic properties computed in this study.

The calculated E_{ads} are consistently negative, confirming that the formation of **APN/$Al_{12}N_{12}$** and **APN/$Al_{12}N_{12}$** complexes are energetically favourable. It can equally be observed from the data in the table that the E_{ads} of complexes formed with **$B_{12}N_{12}$** are higher (about 23 times for **confA** and about 11 times for **confB**) than those formed by **$Al_{12}N_{12}$**. This implies that **confA** forms the most stable adsorption complexes. The E_{ads} values range from −65.12 to −31.55 kcal mol^{-1}, which falls within the range typically associated with chemisorption. This aligns with the formation of strong chemical bonds between **APN** and the nanocage surfaces, further supporting the stability and strength of the interactions.

Additionally, the negative ΔH_{ads} values confirm the exothermic nature of the adsorption processes, indicating that the formation of the **APN**-nanocage complexes is associated with energy-releasing stabilizing interactions. Furthermore, the computed ΔG_{ads} are all negative (−55.19 to −12.82 kcal mol^{-1}), demonstrating that the adsorption of **APN** onto the nanocages is a spontaneous process.

3.3 Topological analysis

To better understand the stability and type of the **APN**/nanocages interactions, Bader's Quantum Theory of Atoms in Molecules (QTAIM)[38] was applied. It analyzes key metrics at the bond critical points (BCPs), including the total electron density ($\rho(r)$), its Laplacian ($\nabla^2\rho(r)$) and the energy densities ($H(r)$, $V(r)$ and $G(r)$). According to QTAIM, specific parameter ranges correspond to different interaction types: non-covalent interactions $\nabla^2\rho(r) > 0$ a.u., $H(r) > 0$ a.u., and $|V(r)|/G(r) < 1$; intermediate interactions (*e.g.*, partial covalent bonds, coordination bonds): $H(r) < 0$ a.u., $\nabla^2\rho(r) > 0$ a.u., and $1 < |V(r)|/G(r) < 2$ and covalent bonds: $H(r) \ll 0$ a.u., $\nabla^2\rho(r) < 0$ a.u., and $|V(r)|/G(r) > 2$. The evaluated QTAIM parameters for the **APN**-nanocage bonds are summarized in Table 2.

Table 2 reveals that for all adsorbate–adsorbent interactions occurring through B–N and Al–N bonds at sites 1 and 2, the QTAIM parameters satisfy the conditions $H(r) < 0$ a.u., $\nabla^2\rho(r) > 0$ a.u., and $1 < |V(r)|/G(r) < 2$, confirming that these interactions are partially covalent. The magnitudes of these topological parameters reveal that the bonds in the **APN–$B_{12}N_{12}$** complexes exhibit significantly stronger covalent character compared to those in the **APN–$Al_{12}N_{12}$** complexes. These findings suggest that **APN** can be easily physisorbed or chemisorbed onto the **$B_{12}N_{12}$** nanocage, while it is primarily physisorbed on the **$Al_{12}N_{12}$** nanocage. In contrast, interactions formed *via* N–H bonds at the same sites exhibit $\nabla^2\rho(r) > 0$ a.u., $H(r) > 0$ a.u., and $|V(r)|/G(r) < 1$, indicating the presence of non-covalent interactions. These outcomes are in line with the molecular graphs (see Fig. 4), which visually depict the bonding patterns between **APN**/nanocages.

The molecular graphs reveal that **APN**'s adsorption is stabilized not only by B–N and Al–N bonds but also through non-covalent interactions. These additional connections contribute to the overall stability of the **APN**/nanocage complexes, further supporting the robustness of the adsorption process.

3.4 Non-covalent interaction (NCI) index analysis

The non-covalent interaction (NCI) index scheme is a powerful tool employed to identify and visualize weak interactions in the **APN**-nanocage complexes. It is based on the reduced density

Table 2 Topological metrics at BCPs **APN**-nanocage bonds in the complexes studied, (all in a.u.), at M06/def2-TZVP level of theory

	APN–$B_{12}N_{12}$				**APN–$Al_{12}N_{12}$**			
Complex	**ConfA**		**ConfB**		**ConfA**		**ConfB**	
Bond	B–N	N–H	B–N	N–H	Al–N	N–H	Al–N	N–H
$\rho(r)$	0.116	0.019	0.117	0.369	0.053	0.021	0.050	0.027
$\nabla^2\rho(r)$	0.141	0.059	0.123	1.079	0.234	0.075	0.210	0.088
$H(r)$	−0.097	0.002	−0.098	0.608	−0.004	0.002	−0.004	0.001
$G(r)$	0.132	0.013	0.129	0.339	0.062	0.017	0.056	0.021
$V(r)$	−0.228	−0.012	−0.227	−0.947	−0.066	−0.015	−0.061	−0.020
$\lvert V(r)\rvert/G(r)$	1.733	−0.878	1.761	−2.797	1.059	−0.889	1.072	−0.946

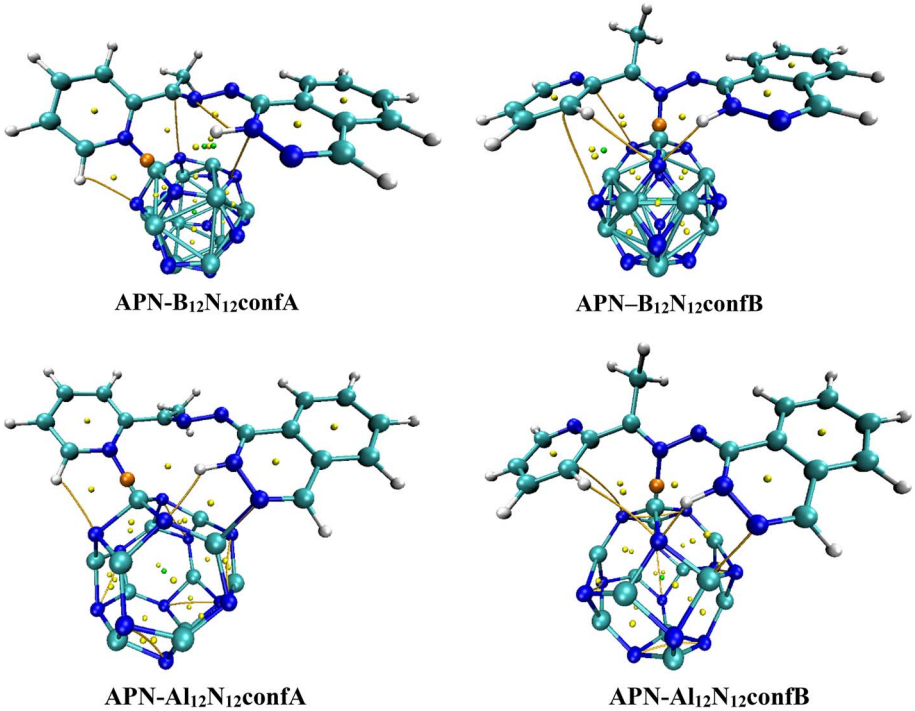

Fig. 4 Molecular graphs characterizing the BCPs of the APN/nanocages interactions.

gradient (RDG), which is calculated from the electron density ($\rho(r)$) and its first derivative ($\nabla\rho(r)$). The RDG-based analysis excels at mapping out weak interactions, such as hydrogen bonds and van der Waals forces and can be seen as a complementary extension of QTAIM theory, offering a more visual and intuitive understanding of these interactions.[39]

$$\mathrm{RDG}(\boldsymbol{r}) = \frac{1}{2(3\pi^2)^{1/3}} \frac{|\nabla\rho(\boldsymbol{r})|}{\rho(\boldsymbol{r})^{4/3}} \tag{10}$$

In NCI framework, the nature and strength of weak interactions are determined by analysing the product of the Hessian matrix's sign(λ_2) and $\rho(r)$. This approach is typically visualized using RDG *vs.* sign(λ_2)$\rho(r)$ plots, which pinpoint specific regions of non-covalent interactions on the molecular surface. The following colour code is used to identify weak interaction types: blue (sign(λ_2)$\rho(r) < 0$) for attractive interactions (covalent and hydrogen bonding), green (sign(λ_2)$\rho(r) \approx 0$) for van der Waals and dispersive interactions and red (sign(λ_2)$\rho(r) > 0$) for repulsive interactions, such as steric clashes.[39,40] Fig. 5 presents both 2D and 3D RDG plots, offering a detailed visualization of the interactions between **APN** and the nanocages.

The RDG plots exhibit distinct spikes corresponding to sign(λ_2)$\rho(r)$ values in the −0.01 to 0.01 a.u. interval, which indicates the existence of weak dispersive interactions, primarily between **APN** and the nanocage surfaces. Spikes at sign(λ_2)$\rho(r) \approx -0.02$ a.u. point to strong hydrogen bonding and partially covalent interactions, consistent with the findings from the QTAIM analysis. Furthermore, spikes at sign(λ_2)$\rho(r) >$ 0.02 a.u. highlight steric clashes, particularly within the aromatic rings of **APN**. The NCI and QTAIM analyses are in strong agreement, confirming that intermediate and non-covalent interactions play a key role in stabilizing the adsorption of **APN** on the outer surfaces of both nanocages.

3.5 Global reactivity descriptors (GRDs)

To shed some light on the reactivity of the investigated molecules, their conceptual DFT-based GRDs were computed at M06/def2-TZVP theoretical level and values enumerated in Table 3.

Molecules with small HOMO–LUMO energy gaps can transition from ground → excited state with relatively low energy input. In contrast, those with large HOMO–LUMO gaps demand significantly more energy for the same transition.[41] The results show that **confA** (with $E_{gap} = 3.56$ eV) and **confB** (with $E_{gap} =$ 4.434 eV) comprising the $\mathbf{B_{12}N_{12}}$ nanocage have lower energy gaps than the monomers **APN** (with $E_{gap} = 4.093$ eV) and $\mathbf{B_{12}N_{12}}$ (with $E_{gap} = 7.492$ eV). A similar pattern can be seen for pristine $\mathbf{Al_{12}N_{12}}$ nanocage and its complexes. Therefore, adsorption of **APN** onto the surfaces $\mathbf{B_{12}N_{12}}$ and $\mathbf{Al_{12}N_{12}}$ increases its reactivity thereby making it more suitable for applications in biological systems.

Chemical potential (μ) reflects how readily a system can exchange electron density with its surroundings, while chemical hardness (η) quantifies a molecule's resistance to such exchange.[42] Generally, molecules with low η and high μ exhibit greater reactivity but lower stability within a chemical system, as they are more prone to participate in electron transfer processes. On this basis, **APN–$\mathbf{B_{12}N_{12}}$confA** (with $\mu = -4.331$ and $\eta = 1.878$) is more reactive and less stable than **APN–**

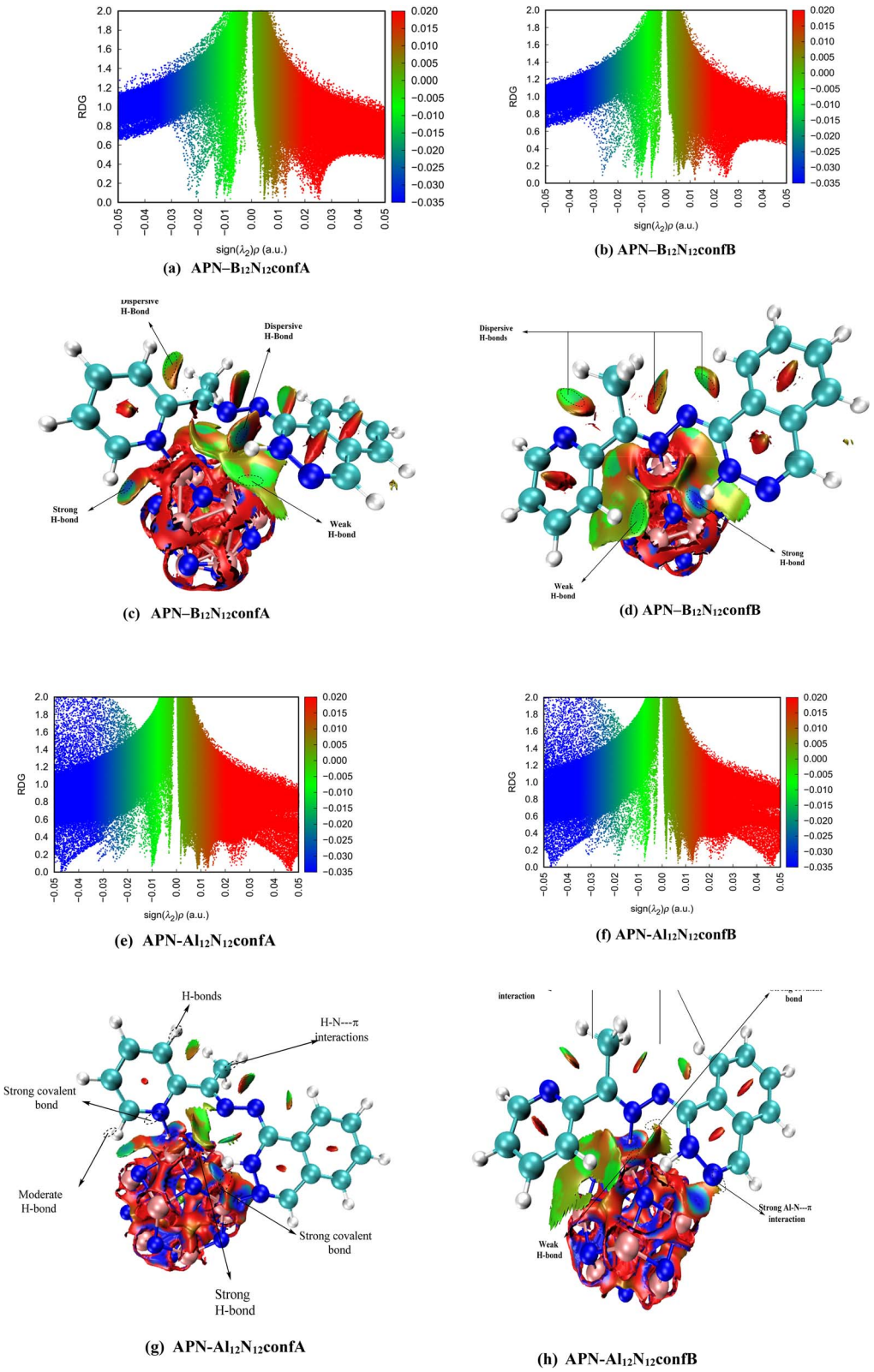

Fig. 5 Panels (a), (b), (e) and (f) display 2D RDG *vs.* sign(λ_2)ρ(r) plots; panels (c), (d), (g) and (h) show 3D RDG isosurfaces, generated with Multiwfn 3.8 using a RDG (s(r)) of 0.05 a.u. and visualized in VMD 1.9. The isosurfaces are color-coded on a red-yellow-green-blue scale with sign(λ_2)ρ(r) values spanning −0.05 to 0.05 a.u.

Table 3 HOMO energy (E_{HOMO}), LUMO energy (E_{LUMO}), chemical potential (μ), HOMO–LUMO energy gap (E_{gap}), electrophilicity (ω), chemical hardness (η), and electron transfer index (ΔN_{max}) (in eV)

Molecule	E_{HOMO}	E_{LUMO}	E_{gap}	μ	η	ω	ΔN_{max}
APN	−5.887	−1.794	4.093	−3.841	2.047	3.604	1.877
$B_{12}N_{12}$	−8.364	−0.872	7.492	−4.618	3.746	2.846	1.233
APN–$B_{12}N_{12}$confA	−6.209	−2.453	3.756	−4.331	1.878	4.994	2.306
APN–$B_{12}N_{12}$confB	−6.706	−2.272	4.434	−4.489	2.217	4.545	2.025
$Al_{12}N_{12}$	−6.877	−2.205	4.672	−4.541	2.336	4.414	1.944
APN–$Al_{12}N_{12}$confA	−5.877	−2.353	3.524	−4.115	1.762	4.805	2.335
APN–$Al_{12}N_{12}$confB	−6.028	−2.277	3.751	−4.153	1.876	4.597	2.214

Table 4 Computed recovery time of the studied complexes (in second (s))

Complex	Recovery time (τ) in s
APN–$B_{12}N_{12}$confA	3.26×10^{-36}
APN–$B_{12}N_{12}$confB	1.05×10^{-33}
APN–$Al_{12}N_{12}$confA	6.681×10^{-53}
APN–$Al_{12}N_{12}$confB	3.23×10^{-42}

Table 5 SWISSAMDE and ADMETlab 3.0 predicted drug-likeness parameters

Parameters	SwissADME	ADMETlab 3.0
M_W (g mol^{-1})	263.3	263.12
nRB	2	2
nHBA	4	5
nHBD	1	1
TPSA Å^2	66.29	66.29
LogP	2.47	2.96
LogS (ESOL)	−3.26	—
Ali LogS (Ali)	−3.12	—
LogS (Silicos-IT)	−6.01	—
Lipinski violation	0	Accepted (0)
Veber violation	0	—

$B_{12}N_{12}$confB (with $\mu = -4.489$ and $\eta = 2.217$). A similar pattern is observed for the **$Al_{12}N_{12}$** nanocage with $\mu = -4.115$ and $\eta = 1.762$ for **confA** and $\mu = -4.153$ and $\eta = 1.876$ for **confB**.

In many cases of molecular reactivity, electron density transfer from a donor to an acceptor species occurs.[42] Molecules with highly positive values of electrophilicity ω and electron transfer index ΔN_{max} have a greater tendency to accept electron density. Data from the table depict that both **APN–$B_{12}N_{12}$confA** (with $\omega = 4.994$ eV and $\Delta N_{max} = 2.306$ eV) and of **APN–$Al_{12}N_{12}$confA** (with $\omega = 4.805$ eV and $\Delta N_{max} = 2.336$ eV) are better electrophiles than of **APN–$B_{12}N_{12}$confB** (with $\omega = 4.545$ eV and $\Delta N_{max} = 2.025$ eV) and of **APN–$Al_{12}N_{12}$confB** (with $\omega = 4.597$ eV and $\Delta N_{max} = 2.214$ eV). Conclusively, the GRDs suggest that **confA** of both **APN–$B_{12}N_{12}$** and **APN–$Al_{12}N_{12}$** are the most are most suitable for biological applications.

3.6 Recovery time

Recovery time (τ) is a key parameter that indicates how swiftly a drug molecule detaches from its carrier,[43,44] making it vital for effective drug delivery mechanisms.[45] Complexes with high adsorption energies tend to be more stable, but they may face challenges in releasing the drug efficiently in biological surroundings.[43] Consequently, a shorter recovery time signifies a faster desorption rate, which enhances the drug's therapeutic effectiveness. In this study, τ was calculated using eqn (11) at room temperature, and the results are presented in Table 4.

$$\tau = {V_o}^{-1}\exp\left(\frac{-E_{ad}}{KT}\right) \quad (11)$$

where, V_o: attempt frequency (10^{12} s^{-1}), E_{ad}: the absolute value of adsorption energy, T: temperature at 298.15 K and K: Boltzmann constant, 2×10^{-3} kcal mol^{-1} K^{-1}.

For each nanocage examined, **confA** exhibits a shorter τ than **confB**. For example, τ for **APN–$B_{12}N_{12}$confA** is approximately 322 times lower than that of **confB**. Likewise, τ for the **APN–$Al_{12}N_{12}$confA** is several hundred times shorter compared to its **confB** counterpart. This indicates that **APN** can be readily desorbed from the **confA**'s of its complexes with both **APN–$B_{12}N_{12}$** and **APN–$Al_{12}N_{12}$** nanocarriers. These rapid recovery times suggest that despite strong binding, **APN** can be efficiently released from both nanocarriers, with **$B_{12}N_{12}$** offering a favorable balance between stability and controlled release.

3.7 Drug-likeness analysis of APN

A drug-like molecule is characterized by possessing acceptable pharmacokinetic and physicochemical parameters.[46,47] Key pharmacokinetic parameters that influence *in vivo* drug activity include systemic exposure, which covers the procedures of absorption, distribution, metabolism, and excretion (ADME); bioavailability, which reflects the extent and rate of drug absorption and metabolism; and elimination, which is determined by the interplay of metabolism, distribution and excretion.[47] To assess the crucial physicochemical properties of **APN**, analyses were performed using the SwissADME.[34] and ADMETlab 3.0.[35] web servers, as detailed in Table 5.

Table 5 includes experimental data alongside predictions derived from Lipinski's Rule of Five (LOF),[48] a widely used guideline for assessing oral drug absorption. According to this rule, compounds are more probable to display poor oral bioavailability if they fail to meet 2 or extra of the subsequent criteria: molecular weight (MW) ≤ 500 Da; octanol–water partition coefficient (LogP) < 5; hydrogen bond acceptors (nHBA) ≤ 10; hydrogen bond donors (nHBD) ≤ 5.[48] Veber's

Table 6 ADMET-related metrics for **APN**, predicted by ADMETLab 3.0[a]

Properties	Score/result
Adsorption	
Caco-2 permeability (log unit)	−4.506
MDCK permeability (cm s^{-1})	−4.572
P-gp inhibitor	+
P-gp substrate	−−−
HIA	−−−
F20%	−−−
F30%	−−−
Distribution	
PPB	95.7%
VDss	0.294
BBB penetration	−−−
Fu	4.1%
Metabolism	
CYP1A2 inhibitor	+++
CYP1A2 substrate	++
CYP2C19 inhibitor	++
CYP2C19 substrate	−−−
CYP2C9 inhibitor	++
CYP2C9 substrate	−−
CYP2D6 inhibitor	−−−
CYP2D6 substrate	−−−
CYP3A4 inhibitor	+
CYP3A4 substrate	−−−
CYP2B6 inhibitor	−−−
CYP2B6 substrate	−−−
CYP2C8 inhibitor	+++
HLM stability	++
Excretion	
Clearance (Ml min^{-1} kg^{-1})	2.819
Half-life (h)	0.929
Toxicity	
hERG blockers	−
DILI	+++
AMES toxicity	+
Human Hepatotoxicity (H-HT)	++
Skin sensitization	+++
Carcinogenicity	+
Eye corrosion	−
Eye irritation	+++
Respiratory toxicity	+++

[a] The prediction probability values are represented using the following: −: 0–0.1; −−: 0.1–0.3; −−−: 0.3–0.5; +: 0.5–0.7; ++: 0.7–0.9; +++: 0.9–1.0. Interpretation: +++ or ++ suggests a higher likelihood of toxicity or defectiveness; −−− or −− indicates a non-toxic or appropriate molecule and + or – represents inconclusive results, requiring further evaluation.

criteria[49] complement these guidelines by focusing on molecular flexibility and polarity: rotatable bonds (nRB) ≤ 10; topological polar surface area (TPSA) ≤ 140 $Å^2$ (indicating better cell permeability).

The results obtained from SwissADME and ADMETlab 3.0 are similar and show no violations to LOF. This compliance with the Lipinski rule demonstrates good oral bioavailability of **APN**. Moreover, the results are also in conformity with the Veber's rule, further confirming its high cell membrane permeability. **APN**'s aqueous solubility was assessed using three SwissADME models: ESOL, Ali and Silicos-IT. The ESOL model predicted a solubility (LogS) of −3.26, and the Ali model predicted a LogS of −3.12, both indicating moderate solubility, which supports the compound's potential for oral administration without major formulation challenges. In contrast, the Silicos-IT model predicted a much lower LogS of −6.01, classifying the compound as poorly soluble. This discrepancy likely reflects the model's sensitivity to molecular flexibility and hydrophobicity. While ESOL and Ali suggest favorable solubility for drug development, the Silicos-IT result highlights the need for caution in formulations where high aqueous solubility is critical. These findings suggest a high probability of oral bioavailability, particularly strong oral absorption and efficient gastrointestinal permeability. The physicochemical properties of **APN** align well with the requirements for achieving favourable pharmacokinetic behaviour in the human body, ensuring they can effectively reach systemic circulation and exert their therapeutic effects.

In addition to physicochemical properties, ADMET-related properties[50] comprising Human Intestinal Absorption (HIA), Caco-2 cell membrane permeability, Madin–Darby Canine Kidney (MDCK) cell membrane permeability, bioavailability (F20% and F30%), Blood–Brain Barrier (BBB) penetration, Volume of Distribution at Steady State (VDss), Plasma Protein Binding (PPB), Fraction Unbound (Fu) in plasma, P-glycoprotein (P-gp) substrates and inhibitors, cytochrome P450 substrates and inhibitors, Drug-Induced Liver Injury (DILI), Human Hepatotoxicity (H-HT), Human Ether-a-Go-Go-Related Gene (hERG) inhibition, AMES toxicity, were evaluated to assess the drug's behaviour in biological systems and their values summarized in Table 6.

Table 6 highlights that **APN** demonstrates favourable intestinal absorption and permeability. It exhibits high Caco-2 cell permeability (−4.506 log unit) and moderate MDCK cell permeability (−4.572 cm s^{-1}), indicating that its absorption in the intestines likely occurs *via* passive transcellular transport crosswise the epithelial lining, as further supported by HIA data. **APN** is also identified as a potential P-gp substrate, an efflux transporter that could enhance its bioavailability, as suggested by F20% and F30% values. However, its potential to inhibit P-gp remains unclear, which could lead to interactions with other P-gp-transported drugs, potentially slowing their absorption. Regarding drug distribution, **APN** shows high plasma protein binding (PPB > 90%), which may limit its access to therapeutic targets. Nevertheless, its predicted volume of distribution (VDss) falls within the optimal 0.04–20 l kg^{-1} interval, indicating substantial tissue distribution rather than concentration in plasma. The low fraction unbound (Fu < 5%) suggests that a smaller proportion of APN remains free in plasma, allowing it to diffuse across cell membranes into tissues, a finding supported by its high blood–brain barrier (BBB) penetration. From an excretion perspective, **APN** has a low clearance rate (∼2.82 ml min^{-1} kg^{-1}) but a short elimination half-life (∼0.9 hours), reducing the likelihood of

significant accretion in the body. *In silico* metabolism profiling indicates that **APN** interacts with multiple cytochrome P450 (CYP) enzymes. It is predicted to be a strong inhibitor of CYP1A2 and CYP2C8, and a moderate inhibitor of CYP2C19, CYP2C9 and CYP3A4. These interactions suggest a high potential for drug–drug interactions, particularly when co-administered with drugs that are metabolized by these enzymes. In terms of substrate liability, **APN** is predicted to be a substrate of CYP1A2, but not of CYP2C9, CYP2C19, CYP2D6, CYP2B6 or CYP3A4, indicating a limited chances of **APN** metabolism by these enzymes. Despite the weak CYP3A4 inhibition, the absence of CYP3A4 substrate behaviour may reduce the risk of rapid hepatic clearance. **APN** demonstrates moderate human liver microsomal (HLM) stability, suggesting that it is not rapidly metabolized and may exhibit favourable hepatic metabolic stability. However, the predicted multi-CYP inhibition, especially of CYP1A2 and CYP2C8, highlights the need for further *in vitro* metabolic profiling of **APN**.

Based on the predicted toxicological parameters, **APN** may pose an elevated risk of respiratory toxicity, skin sensitization, eye irritation, and liver injury. It also exhibits moderate human hepatotoxicity but shows low risks of carcinogenicity, hERG inhibition, eye corrosion, and AMES toxicity. These findings suggest that **APN** is a safe molecule for use in the subcutaneous treatment of filariasis (onchocerciasis).

4. Conclusion

This research explores the likelihood of $\mathbf{B_{12}N_{12}}$ and $\mathbf{Al_{12}N_{12}}$ nanocages as drug delivery systems for the anti-onchocercal compound 1-(phthalazin-1(2*H*)-one)[(pyridin-2-yl)ethylidene] hydrazone (**APN**). DFT calculations were conducted at the M06/def2-SVP and M06/def2-TZVP levels for energy minimization and property calculations, respectively. Molecular Electrostatic Potential (MESP) analysis identified two potential adsorption sites on **APN**: the pyridine nitrogen (**confA**) and the azomethine nitrogen (**confB**). Thermochemical analysis confirmed that the formation of **APN**-nanocage complexes is energetically favourable, exothermic and spontaneous, with **confA** complexes demonstrating the highest stability. Global reactivity studies indicate that complexation, particularly *via* **confA**, significantly enhances reactivity, as evidenced by lower HOMO–LUMO energy gaps and favourable electron transfer properties. QTAIM and NCI analyses revealed that the primary interactions in the complexes are intermediate and non-covalent. **APN** exhibits a promising drug-like profile, making it a strong candidate for further development as an orally bioavailable drug. The findings demonstrate that $\mathbf{B_{12}N_{12}}$ and $\mathbf{Al_{12}N_{12}}$ nanocages have significant potential as effective drug transport systems for **APN** in the treatment of onchocerciasis.

Data availability

The data that support the findings of this study are included in the ESI† of this article.

Conflicts of interest

The authors declare no conflicts of interest regarding the publication of this paper.

Acknowledgements

The authors are thankful to the Ministry of Higher Education of Cameroon for their support to University Lecturers.

References

1 G. Gebrezgabiher, Z. Mekonnen, D. Yewhalaw and A. Hailu, Reaching the last mile: main challenges relating to and recommendations to accelerate onchocerciasis elimination in Africa, *Infectious Diseases of Poverty*, 2019, **8**, 60.
2 J. N. Siewe Fodjo, et al., Onchocerciasis in the Ntui Health District of Cameroon: epidemiological, entomological and parasitological findings in relation to elimination prospects, *Parasites Vectors*, 2022, **15**, 444.
3 A. Ngwewondo, I. Scandale and S. Specht, Onchocerciasis drug development: from preclinical models to humans, *Parasitol. Res.*, 2021, **120**, 3939–3964.
4 A. Prost, The different types of human onchocerciasis in west Africa, *Ann. Parasitol. Hum. Comp.*, 1980, **55**, 239–245.
5 E. W. Cupp, M. Sauerbrey and F. Richards, Elimination of human onchocerciasis: history of progress and current feasibility using ivermectin (Mectizan®) monotherapy, *Acta Trop.*, 2011, **120**, S100–S108.
6 A. Hopkins, Onchocerciasis then and now: achievements, priorities and challenges, *Community Eye Health*, 2017, **30**, 92–95.
7 J. N. Yong, F. Majoumo-Mbe, M. Samje and E. N. Nfor, Synthesis, Molecular Structure and Anti-Onchocercal Studies of 1-(Phthalazin-1(2H)-one)[(Pyridin-2-yl)ethylidene] hydrazone, *Int. J. Org. Chem.*, 2016, **06**, 77–84.
8 M. Y. Osei-Atweneboana, J. K. Eng, D. A. Boakye, J. O. Gyapong and R. K. Prichard, Prevalence and intensity of Onchocerca volvulus infection and efficacy of ivermectin in endemic communities in Ghana: a two-phase epidemiological study, *Lancet*, 2007, **369**, 2021–2029.
9 S. Lustigman and J. P. McCarter, Ivermectin Resistance in Onchocerca volvulus: Toward a Genetic Basis, *PLoS Neglected Trop. Dis.*, 2007, **1**, e76.
10 A. Nimibofa, E. A. Newton, A. Y. Cyprain and W. Donbebe, Fullerenes: Synthesis and Applications, *J. Mater. Sci. Res.*, 2018, **7**, 22.
11 H. Y. Ammar, K. M. Eid and H. M. Badran, TM-doped $Mg_{12}O_{12}$ nano-cages for hydrogen storage applications: theoretical study, *Results Phys.*, 2022, **35**, 105349.
12 A. Soltani, et al., Serine adsorption through different functionalities on the $B_{12}N_{12}$ and Pt-$B_{12}N_{12}$ nanocages, *Mater. Sci. Eng., C*, 2018, **92**, 216–227.
13 F. Shafiei, S. M. Hashemianzadeh and Y. Bagheri, Insight into the encapsulation of gemcitabine into boron-nitride nanotubes and gold cluster triggered release: a molecular dynamics simulation, *J. Mol. Liq.*, 2019, **278**, 201–212.

14 A. Soltani, M. T. Baei, E. Tazikeh Lemeski, S. Kaveh and H. Balakheyli, A DFT study of 5-fluorouracil adsorption on the pure and doped BN nanotubes, *J. Phys. Chem. Solids*, 2015, **86**, 57–64.
15 N. Abdolahi, et al., Adsorption of Celecoxib on $B_{12}N_{12}$ fullerene: spectroscopic and DFT/TD-DFT study, *Spectrochim. Acta, Part A*, 2018, **204**, 348–353.
16 E. W. Askew, G. L. Dohm and R. L. Huston, Fatty acid and ketone body metabolism in the rat: response to diet and exercise, *J. Nutr.*, 1975, **105**, 1422–1432.
17 Y. Cao, et al., Penicillamine functionalized $B_{12}N_{12}$ and $B_{12}CaN_{12}$ nanocages act as potential inhibitors of proinflammatory cytokines: a combined DFT analysis, ADMET and molecular docking study, *Arabian J. Chem.*, 2021, **14**, 103200.
18 H. I. Feinstein, Diagonal relationships - descriptive or theoretical?, *J. Chem. Educ.*, 1984, **61**, 128.
19 C. T. Tsapi, et al., Exohedral Adsorption of N-(4-Methoxybenzylidene) Isonicotinohydrazone Molecule onto $X_{12}N_{12}$ Nanocages (Where X=B and Al) and the Effect on Its NLO Properties by DFT and TD-DFT, *J. Chem.*, 2023, **2023**, 1–15.
20 E. G. Lewars, *Computational Chemistry*, Springer Netherlands, Dordrecht, 2011, DOI: 10.1007/978-90-481-3862-3.
21 F. Neese, Software update: the ORCA program system—version 5.0, *Wiley Interdiscip. Rev.: Comput. Mol. Sci.*, 2022, **12**, e1606.
22 F. Neese, F. Wennmohs, U. Becker and C. Riplinger, The ORCA quantum chemistry program package, *J. Chem. Phys.*, 2020, **152**, 224108.
23 S. Portmann and H. P. Lüthi, MOLEKEL: An Interactive Molecular Graphics Tool: Computational Chemistry Column, *Chimia*, 2000, **54**, 766.
24 M. D. Hanwell, et al., Avogadro: an advanced semantic chemical editor, visualization, and analysis platform, *J. Cheminf.*, 2012, **4**, 17.
25 E. G. Hohenstein, S. T. Chill and C. D. Sherrill, Assessment of the Performance of the M05-2X and M06-2X Exchange-Correlation Functionals for Noncovalent Interactions in Biomolecules, *J. Chem. Theory Comput.*, 2008, **4**, 1996–2000.
26 J. Laun, D. Vilela Oliveira and T. Bredow, Consistent Gaussian basis sets of double- and triple-zeta valence with polarization quality of the fifth period for solid-state calculations: fifth period for solid-state calculations, *J. Comput. Chem.*, 2018, **39**, 1285–1290.
27 Y. Zhao and D. G. Truhlar, The M06 suite of density functionals for main group thermochemistry, thermochemical kinetics, noncovalent interactions, excited states, and transition elements: two new functionals and systematic testing of four M06-class functionals and 12 other functionals, *Theor. Chem. Acc.*, 2008, **120**, 215–241.
28 R. A. Kendall and H. A. Früchtl, The impact of the resolution of the identity approximate integral method on modern ab initio algorithm development, *Theor. Chem. Acc.*, 1997, **97**, 158–163.
29 S. Simon, M. Duran and J. J. Dannenberg, How does basis set superposition error change the potential surfaces for hydrogen-bonded dimers?, *J. Chem. Phys.*, 1996, **105**, 11024–11031.
30 H. Kruse and S. Grimme, A geometrical correction for the inter- and intra-molecular basis set superposition error in Hartree-Fock and density functional theory calculations for large systems, *J. Chem. Phys.*, 2012, **136**, 154101.
31 T. Lu and Q. Chen, Shermo: a general code for calculating molecular thermochemistry properties, *Comput. Theor. Chem.*, 2021, **1200**, 113249.
32 P. Hobza, Calculations on Noncovalent Interactions and Databases of Benchmark Interaction Energies, *Acc. Chem. Res.*, 2012, **45**, 663–672.
33 T. Lu and F. Chen, Multiwfn: a multifunctional wavefunction analyzer, *J. Comput. Chem.*, 2012, **33**, 580–592.
34 A. Daina, O. Michielin and V. Zoete, SwissADME: a free web tool to evaluate pharmacokinetics, drug-likeness and medicinal chemistry friendliness of small molecules, *Sci. Rep.*, 2017, **7**, 42717.
35 L. Fu, et al., ADMETlab 3.0: an updated comprehensive online ADMET prediction platform enhanced with broader coverage, improved performance, API functionality and decision support, *Nucleic Acids Res.*, 2024, **52**, W422–W431.
36 M. T. Baei, Adsorption of the urea molecule on the B$_{12}$N$_{12}$ nanocage, *Turk. J. Chem.*, 2014, **38**, 531–537.
37 J. B. Condon, *Surface Area and Porosity Determinations by Physisorption*, Elsevier, 2006, DOI: 10.1016/B978-0-444-51964-1.X5000-6.
38 S. Esser, The Quantum Theory of Atoms in Molecules and the Interactive Conception of Chemical Bonding, *Philos. Sci.*, 2019, **86**, 1307–1317.
39 T. Lu and Q. Chen, Visualization Analysis of Weak Interactions in Chemical Systems, in *Reference Module in Chemistry, Molecular Sciences and Chemical Engineering*, B9780128219782000763, Elsevier, 2023, DOI: 10.1016/B978-0-12-821978-2.00076-3.
40 E. R. Johnson, et al., Revealing Noncovalent Interactions, *J. Am. Chem. Soc.*, 2010, **132**, 6498–6506.
41 M. R. Jalali Sarvestani and R. Ahmadi, Trinitroanisole Adsorption on the Surface of Boron Nitride Nanocluster ($B_{12}N_{12}$): A Computational Study, *J. Water Environ. Nanotechnol.*, 2020, **5**, 34–44.
42 L. Domingo, M. Ríos-Gutiérrez and P. Pérez, Applications of the Conceptual Density Functional Theory Indices to Organic Chemistry Reactivity, *Molecules*, 2016, **21**, 748.
43 M. Sheikhi, S. Kaviani, F. Azarakhshi and S. Shahab, Superalkali X_3O (X = Li, Na, K) doped $B_{12}N_{12}$ nano-cages as a new drug delivery platform for chlormethine: a DFT approach, *Comput. Theor. Chem.*, 2022, **1212**, 113722.
44 Y. Yang and N. Ostadhosseini, A theoretical investigation on the mercaptopurine drug interaction with boron nitride nanocage: solvent and density functional effect, *Phys. E*, 2021, **125**, 114337.
45 H. Yahyaei, et al., Predicting adsorption behavior of Triacanthine anticancer drug with pure $B_{12}N_{12}$ nano-cage: a theoretical study, *J. Indian Chem. Soc.*, 2023, **100**, 100812.

46 I. Ahmad, H. Khan and G. Serdaroğlu, Physicochemical properties, drug likeness, ADMET, DFT studies, and in vitro antioxidant activity of oxindole derivatives, *Comput. Biol. Chem.*, 2023, **104**, 107861.

47 T. Vallianatou, C. Giaginis and A. Tsantili-Kakoulidou, The Impact of Physicochemical and Molecular Properties in Drug Design: Navigation in the "Drug-Like" Chemical Space, in *GeNeDis 2014*, ed. P. Vlamos and A. Alexiou, Springer International Publishing, Cham, 2015, vol. 822, pp. 187–194.

48 C. A. Lipinski, F. Lombardo, B. W. Dominy and P. J. Feeney, Experimental and computational approaches to estimate solubility and permeability in drug discovery and development settings, *Adv. Drug Delivery Rev.*, 2001, **46**, 3–26.

49 D. F. Veber, et al., Molecular Properties That Influence the Oral Bioavailability of Drug Candidates, *J. Med. Chem.*, 2002, **45**, 2615–2623.

50 Y. Yasugi, Y. Shirasaka and I. Tamai, Quantitative analysis of the impact of membrane permeability on intestinal first-pass metabolism of CYP3A substrates, *Biopharm. Drug Dispos.*, 2024, **45**, 3–14.